



Behavior of high-entropy W-rich alloys $W_x(TaVCrTi)_y$ under He^+ irradiation

Hongjing Cui, Ning Liu*, Laima Luo, Yue Xu, Jigui Cheng, Yucheng Wu

School of Materials Science and Engineering, Hefei University of Technology, Hefei 230009, China



ARTICLE INFO

Keywords:

High-entropy alloys
Tungsten
Radiation effects
 He^+

ABSTRACT

A group of high-entropy W-rich (HE-W) alloys were investigated as potential divertor materials in this study. Pure W and four HE-W alloys: $W_{90}(TaVCrTi)_{10}$, $W_{80}(TaVCrTi)_{20}$, $W_{70}(TaVCrTi)_{30}$, and $W_{60}(TaVCrTi)_{40}$ were manufactured by mechanical alloying and spark plasma sintering. The HE-W alloys showed the body-centered cubic structure with W-based and Ti-rich grains. The HE-W alloys had the ultrafine grain size, which were much finer than that of pure W. The HE-W alloys exhibited excellent surface stability under He^+ irradiation. Even under an irradiation fluence of 0.9×10^{25} ions/m², the surface of the HE-W alloys remained nearly flat. The excellent He^+ surface stability of the HE-W alloys was due to their self-healing mechanism and the effect of the irradiation temperature on the irradiation damage was not significant.

1. Introduction

Because of its remarkable properties, such as high melting temperature, good thermal conductivity, and low sputtering yield, W is considered as a prospective component of plasma facing materials (PFMs) [1–5]. However, for application as the armor material in divertor components, W-based materials should be resistant to helium (He) irradiation for long-term operations [3, 6, 7]. Therefore, further development of W materials is required to work in such serious environment.

Solid solution strengthening [8–11] belongs to strengthening methods applicable for W-based materials. However, researchers mainly focused on the binary W alloys. The design of high-entropy alloys (HEAs) [12], has inspired the development of novel W-based materials. HEAs usually have five or more principal elements with equiatomic or near-equiatomic contents, which can be attributed to their high configurational entropy. The four main effects observed in HEAs are [13]: (1) the high entropy effect [14], (2) the lattice distortion effect [15], (3) the sluggish diffusion effect [16], and (4) the cocktail effect [17]. These effects endow HEAs with excellent physical and mechanical properties. The two key characteristics of HEAs, microstructural stability [18] and excellent mechanical properties [19], make HEAs suitable for application in PFM under irradiation environments. Kumar N.K. et al. [18] studied the microstructural stability of FeNiMnCr HEA and two types of traditional austenitic steels under ion irradiation. Above 400 °C, FeNiMnCr HEA showed better phase stability than the two austenitic

steels under ion irradiation. Void formation was not observed under any irradiation condition in the FeNiMnCr HEA. Thus, the HEAs showed better swelling resistance than the conventional steels. Takeshi Nagase et al. discussed the irradiation resistance of HEAs from the perspective of simulations and experiments. Computer simulations performed in Ref. [20] indicated that HEAs exhibit a self-healing mechanism, which contributes to their high irradiation resistance. The experimental results for ZrHfNb [20] and CoCuCrFeNi [21] were in good agreement with theoretical simulations. However, only a few studies have focused on the performance of HEAs under fusion reactor conditions. Therefore, it is imperative to study the He^+ irradiation behavior of HEAs.

To induce the four core effects in W-based HEAs, four elements other than W can be added. The amount of W is higher than the sum of the amounts of the other elements. This can maintain the high melting point of the W-based materials as much as possible to adjust it to the operating temperature window (OTW) [22]. These high-entropy W-rich alloy, namely HE-W alloys, can be considered as non-equiatomic HEAs. The composition of such non-equiatomic HEAs is almost the same as that of traditional alloys, but the four core effects of HEAs still play an important role [23–27]. The other four elements are selected based on the basis of previous studies on refractory HEAs and binary W alloys. Refractory HEAs consist of refractory elements, and most of them have a body-centered cubic (BCC) structure, such as WNbMoTaV [28], MoTaVWZr [29], and WMoVCrTa [31]. With further studies, researchers hope to decrease the density and improve the room

* Corresponding author.

E-mail address: 2042845889@qq.com (N. Liu).

temperature ductility of refractory HEAs by mixing light metals, such as Ti and Al. Some mixing refractory HEAs, such as NbTiVTaAl [25], TiNbMoTaW [32], TiZrNbMoV [33], ZrNbAlTiV [34], and TaNbHfZrTi [35], have been developed. With an increase the compression strain from <10% [30, 36] to >50% [25, 35], the density of these alloys decreases and the ductility becomes significantly higher than that of conventional refractory HEAs. Some of the elements used in refractory HEAs have been widely studied as binary W alloys, such as W-Ta [8], W-V [9], W-Cr [10], and W-Ti [11]. Therefore, the HE-W alloys can be referred to as $W_x(TaVCrTi)_y$, where x is the W content (at%) and y is the sum of the Ta, V, Cr, and Ti contents in at%.

In this study, four HE-W alloys, namely $W_{90}(TaVCrTi)_{10}$, $W_{80}(TaVCrTi)_{20}$, $W_{70}(TaVCrTi)_{30}$ and $W_{60}(TaVCrTi)_{40}$, were prepared using the mechanical alloying and spark plasma sintering (SPS) methods. The structures, mechanical properties and He^+ irradiation resistance of the four HE-W alloys were investigated. For comparison, pure W was also fabricated and characterized.

2. Materials and methods

Powder metallurgy was used to manufacture the four HE-W alloys and pure W. The short names, compositions and calculated melting temperatures of the five materials are listed in Table 1. It can be observed from the table that the calculated melting temperatures of all the four HE-W alloys were higher than 3000 K. The particle sizes of the W, Ta, V, Cr, and Ti raw powders were 1, 45, 45, 45, and 45 μm , respectively. The powders had a purity of 99.9%. All powders were produced by Xiamen Golden Egret Special Alloy Co., Ltd., PR China. The manufacturing process involved two steps: mechanical alloying and SPS (SINTERLAND LABOX-350). Tungsten carbide balls and bowls were used during mechanical alloying. The ball-to-powder ratio was 10:1, and the milling speed and milling time were 400 rpm and 25 h, respectively. A high-purity argon gas atmosphere was used to prevent oxidation, and no process control agent was used. During the SPS process, the powders were loaded into a cylindrical graphite mold with a diameter of 20 mm. Temperature was increased to 600 $^{\circ}C$ in 10 min with a holding time of 5 min and was then increased to 1450 $^{\circ}C$ in 10 min and held for 5 min. Finally, the furnace was cooled to room temperature. Sintering was performed at a pressure of 40 MPa under vacuum. The sintered blanks were cut into the desired samples using electrical discharge wire machining. X-ray diffraction (XRD, PANalytical X-Pert PRO MPD), scanning electron microscopy (SEM, Gemini 500) with energy dispersive X-Ray spectroscopy (EDS), and field-emission transmission electron microscopy (FETEM, JEM-2100F) were used for the phase analysis of the as-sintered materials.

The He^+ irradiation test was carried out in linear plasma in a plasma-surface interaction system under extreme conditions at the Hefei University of Technology, China [37]. The sintered blanks were cut into 10 mm \times 10 mm \times 1 mm, which were then mechanically polished to a mirror finish. All the samples were exposed to 60-eV He^+ ion irradiation with a flux of 5×10^{21} ions/($m^2 s$). Two types of irradiation fluences were set: (I) 3×10^{24} ions/ m^2 with 10-min duration as the low fluence, and (II) 0.9×10^{25} ions/ m^2 with 30 min duration as the high fluence. During the test, a thermocouple was used to hold the back of the samples to measure the temperature. The changes in the surface morphology of

the sample changes were also observed by SEM with EDS. To measure the changes in the surface roughness of samples after the irradiation, a 3D laser scanning confocal microscope (KEYENCE VK-X250) was used before and after irradiation tests. The thermal diffusivity of the samples was tested using a laser thermal conductivity testing instrument (NETZSCH LFA 457 MicroFlash). All the analysis results obtained before the irradiation test are marked as pristine.

3. Results and discussion

The XRD patterns of the five as-sintered materials are shown in Fig. 1. Fig. 1a shows the XRD wide scans of the five as-sintered materials, where the dotted lines indicated the positions of the four peaks in the standard XRD pattern of W. All the four HE-W alloys showed only four peaks, which are similar to those of W. The four HE-W alloys had a single-phase BCC structure. Fig. 1b shows the magnified W (110) peaks of the samples. These peaks confirm that the four HE-W alloys had the single-phase BCC structure.

SEM-EDS analysis was performed to analyze the elemental distribution of the HE-W alloys, and the results were shown in Fig. 2. Fig. 2a shows the SEM-BSE image of the $W_{70}\text{-M30}$ alloy. Fig. 2b shows the typical EDS profiles of the bright and dark grains. The EDS results indicated that the bright grains in Fig. 2a were W-based grains, and the dark grains in Fig. 2a were Ti-rich grains. The $W_{70}\text{-M30}$ alloy showed much finer grains than W, as shown in Fig. 2d. The SEM-EDS results of the $W_{60}\text{-M40}$, $W_{80}\text{-M20}$, and $W_{90}\text{-M10}$ alloys were the same as those of the $W_{70}\text{-M30}$ alloy. Grain size analysis was performed on the five materials, and the grain sizes of the W-based and Ti-rich grains in the HE-W alloys were also determined. The results were summarized in Table 2. The HE-W alloys showed ultrafine grains, whose size decreased with an increase in the Ta, V, Cr, and Ti contents. Thus, the $W_{60}\text{-M40}$ alloy showed the finest grains among all the five materials investigated in this study. However, the difference in the grain sizes of the four HE-W alloys was not significant.

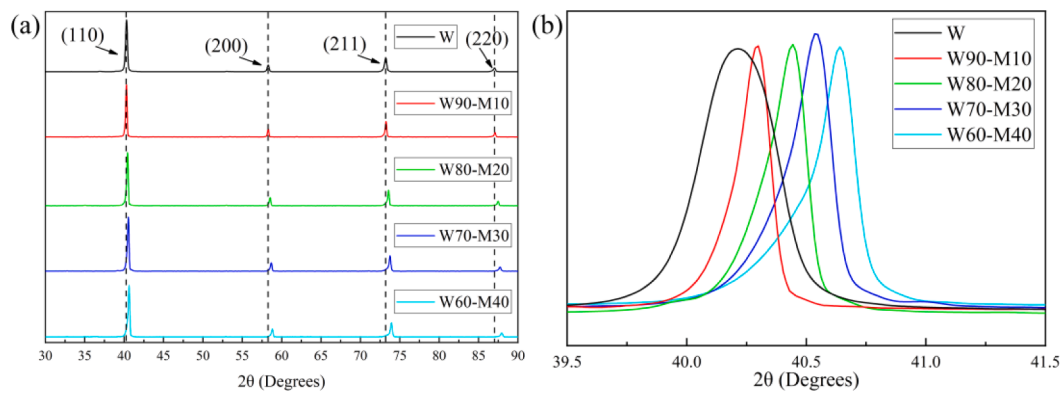
The phase structures of the four HE-W alloys were further analyzed by obtaining their bright-field (BF) and dark-field (DF) images, selected area electron diffraction (SAED) patterns, and EDS mapping profiles. The TEM analysis results for the $W_{70}\text{-M30}$ alloy are shown in Fig. 3. Two grains were analyzed. On the basis of the EDS mapping analysis results (Fig. 3b), grain c in Fig. 3a was identified to be a Ti-rich grain, while grain d was identified to a W-based grain. This is consistent with the SEM-EDS analysis results shown in Fig. 2. The DF and SAED results indicated that the two grains had the BCC structure. The TEM analysis of the $W_{60}\text{-M40}$, $W_{80}\text{-M20}$, and $W_{90}\text{-M10}$ alloys were also carried out, and the results were similar to those shown in Fig. 3.

The surfaces of the irradiated samples were observed using SEM, as shown in Fig. 4. As compared to pure W, all the four HE-W alloys showed excellent surface stability under He^+ irradiation, as shown in Fig. 4. Under low fluence irradiation, the tendril structure appeared on the surface of W, as shown in Fig. 4a. When the irradiation fluence was increased, the fuzz structure could be observed on the surface of W, as shown in Fig. 4b. HE-W alloys showed a nearly flat surface irrespective of the irradiation fluence, as shown in Fig. 4c-j.

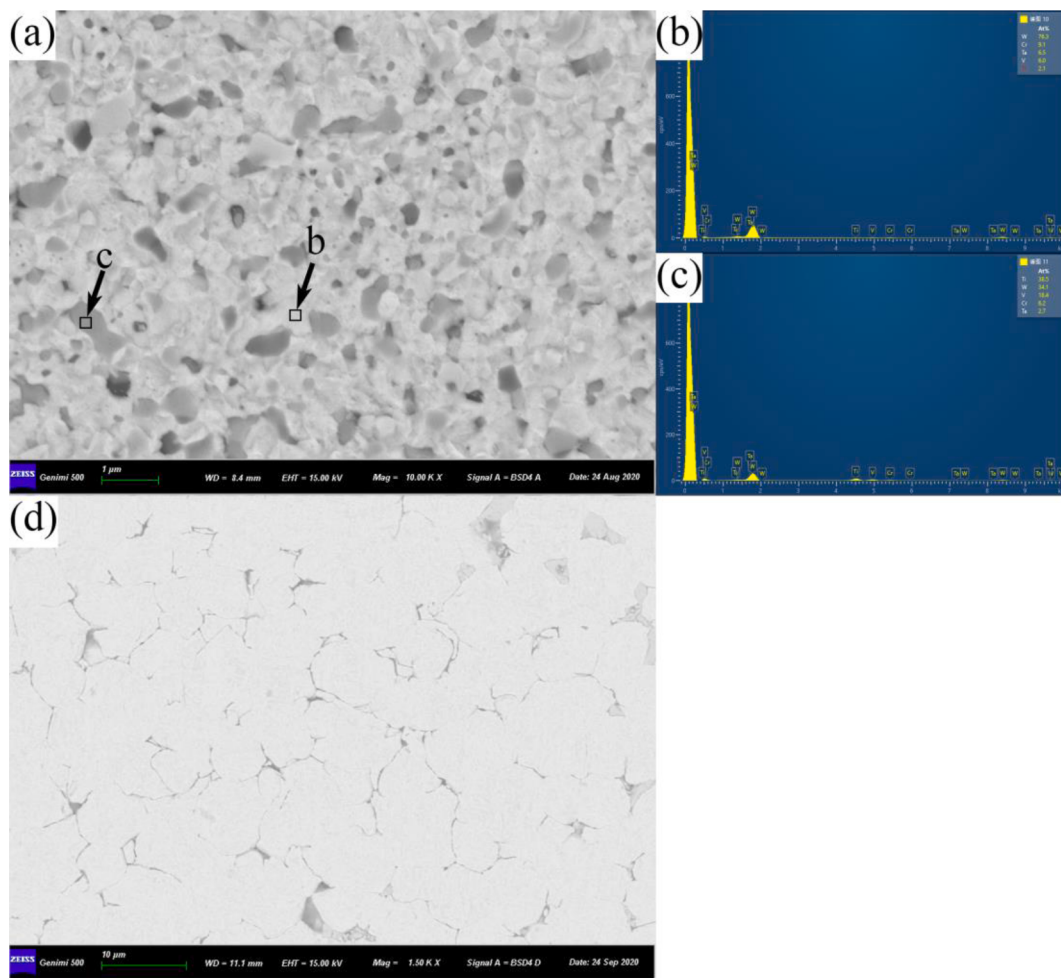
As can be observed from the images shown in Fig. 4, some grains (marked with black arrows in Fig. 4c-j) in the HE-W alloys had a tendril

Table 1
Short name, compositions and calculated melting temperatures of five materials.

Material	Short name	Composition in at.%					Composition in wt.%					Calculated melting temperature (K)
		W	Ta	V	Cr	Ti	W	Ta	V	Cr	Ti	
Pure W	W	100	0	0	0	0	100	0	0	0	0	3683
$W_{90}(TaVCrTi)_{10}$	W90-M10	90	2.5	2.5	2.5	2.5	95.23	2.60	0.73	0.75	0.69	3552
$W_{80}(TaVCrTi)_{20}$	W80-M20	80	5	5	5	5	89.86	5.53	1.56	1.59	1.46	3421
$W_{70}(TaVCrTi)_{30}$	W70-M30	70	7.5	7.5	7.5	7.5	83.80	8.84	2.49	2.54	2.34	3291
$W_{60}(TaVCrTi)_{40}$	W60-M40	60	10	10	10	10	76.88	12.61	3.55	3.62	3.34	3160

**Fig. 1.** XRD patterns of the samples

(a) Wide scans of the samples, (b) magnified W (110) peak in (a) for the samples.

**Fig. 2.** SEM-EDS analysis of the W70-M30 alloy and pure W

(a) SEM-BSE image of the W70-M30 alloy, (b) EDS analysis of grain b in (a), (c) EDS analysis of grain c in (a), and (d) SEM-BSE image of pure W.

structure. The EDS analysis results (Table 3) indicated that these grains were Ti-rich, which is consistent with the SEM-EDS and TEM results of the HE-W alloys. The EDS analysis of the alloys before and after the irradiation test was also carried out under $200 \times$ magnification, and the results are summarized in Table 4. Under this magnification, the detection zone of EDS could cover a sufficiently large area to study the changes in the elemental composition of the alloys after the irradiation. It can be observed from the table that for all the four alloys, the Ti content decreased with an increase in the irradiation fluence, which

indicates that Ti was sputtered during the irradiation process. As the Ti-rich grains suffered serious damage under the irradiation, it can be stated that the Ti spurt was mainly from these grains. Thus, the addition of Ti improves the surface stability of W-based materials; however, Ti-rich grains can cause sufficient damage to HE-W alloys.

To further analyze the surface irradiation damage of the five materials, their surface morphologies were examined using a 3D laser scanning confocal microscope before and after the irradiation. The precision of these measurements was $\leq \pm 0.2\%$. As can be observed from the

Table 2
Grain sizes and area ratios of the five materials.

Material W	Grain \	Average grain size (μm)	Area ratio (%) \
W90-M10	Ti-enriched \	0.166	17.27
	W-enriched	0.297	82.73
	Total	0.274	\
W80-M20	Ti-enriched	0.187	17.47
	W-enriched	0.284	82.53
	Total	0.267	\
W70-M30	Ti-enriched	0.182	18.70
	W-enriched	0.280	81.30
	Total	0.262	\
W60-M40	Ti-enriched	0.196	18.93
	W-enriched	0.274	81.07
	Total	0.259	\

roughness measurement results (Table 5), before the irradiation, the surface roughness of all the five materials was nearly the same. The surface roughness of the five materials increased after the irradiation irrespective of the fluence. With the addition of alloying elements, the irradiation damage of the HE-W alloys first decreased and then increased. This indicates that the damage of the W70-M30 alloy was the lowest.

For conventional W alloys, grain refinement usually plays a major

role in enhancing the He^+ irradiation resistance [38, 39]. This mechanism still affects the irradiation resistance of the HE-W alloys. Moreover, the self-healing mechanism of HEAs, i.e., the amorphization-recrystallization process, can play an important role in improving the He^+ irradiation resistance of HE-W alloy [20, 21]. The mixing of various elements in HEAs usually generates high atomic-level stress, and the atoms in crystals show a disordered arrangement. These mechanisms lead to amorphization and the subsequent recrystallization under irradiation in HEAs [20, 21]. This significantly reduces the number of defects in HEAs, which hinders the formation of He bubbles

Table 3
EDS results of the grains marked with black arrows in Fig. 4.

Material	Figure	Composition in at.%				
		W	Ta	V	Cr	Ti
W90-M10	c	75.1	8	5.9	3.9	7.2
	d	76.5	8.2	4.2	4.2	5.6
W80-M20	e	52.8	6.3	11.3	6.9	22.7
	f	63.6	9.2	8.5	6.2	12.6
W70-M30	g	38.5	5.9	13.5	5.7	36.5
	h	32.3	11.1	14.1	6.8	35.7
W60-M40	i	26.1	4.8	18.9	6.7	43.6
	j	33.5	6.7	16.5	8	35.4

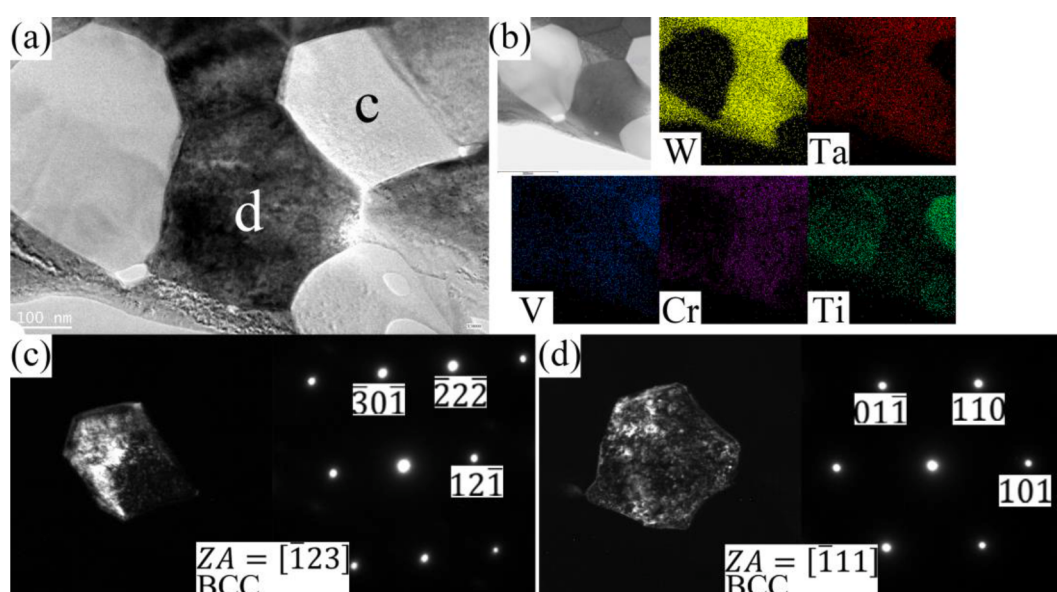


Fig. 3. TEM analysis of the W70-M30 alloy

(a) BF image, (b) EDS mapping results, (c) DF image and SAED pattern of grain c in (a), (d) DF image and SAED pattern of grain d in (a).

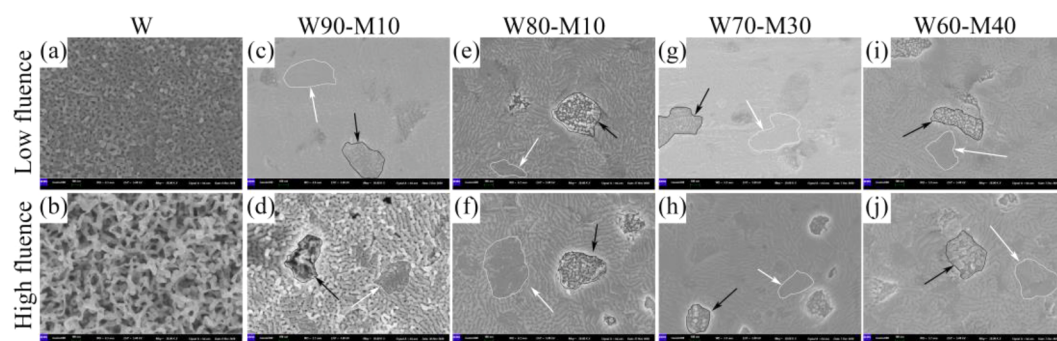


Fig. 4. Surface SEM images of the samples after He^+ irradiation

(a) W low fluence, (b) W high fluence, (c) W90-M10 low fluence, (d) W90-M10 high fluence, (e) W80-M20 low fluence, (f) W80-M20 high fluence, (g) W70-M30 low fluence, (h) W70-M30 high fluence, (i) W60-M40 low fluence, and (j) W60-M40 high fluence.

Table 4

EDS results of the four HE-W alloys under 200 × magnification.

Material	Stage	Composition in at.%				
		W	Ta	V	Cr	Ti
W90-M10	Pristine	88.2	2.7	2.7	3.2	3.1
	Low fluence	88.7	2.6	2.7	3.1	3
	High fluence	90.4	2.7	2.1	2.4	2.4
W80-M20	Pristine	78.1	5.4	5.5	5	5.9
	Low fluence	78.7	5.7	5.5	5.1	5
	High fluence	80.1	5.7	4.9	4.7	4.5
W70-M30	Pristine	67.9	8.1	7.5	7.5	9
	Low fluence	68.6	8.5	7.3	7.2	8.5
	High fluence	68.9	8.9	7.1	7.1	8
W60-M40	Pristine	56.9	10.4	10.8	9.8	12.1
	Low fluence	59.4	10.6	10	9.7	10.3
	High fluence	59.5	10.7	10.1	9.5	10.2

Table 5

Surface roughness of the five materials in different states.

Materials	Surface roughness, Sa (μm)		
	Pristine	Low fluence	High fluence
W	0.011	0.080	0.126
W90-M10	0.005	0.010	0.012
W80-M20	0.005	0.008	0.010
W70-M30	0.005	0.006	0.007
W60-M40	0.005	0.007	0.009

[40]. The irradiation-induced amorphization-recrystallization process has been reported in conventional materials, such as binary alloy systems [41, 42] and intermetallic compounds [43, 44]. However, conventional materials show smaller atom-level stress and more ordered atomic arrangement than HEAs. Thus, the amorphization-recrystallization process shows less effect on the irradiation resistance of conventional materials than on that of HEAs. For the HE-W alloys in this work, with the an increase in the Ta, V, Cr and Ti contents, the atomic-level stress increased, and more crystals showed a disordered atomic arrangement. This made the amorphization-recrystallization process easier. However, the sputtering of the Ti-rich grains still affected the surface irradiation damage of the HE-W alloys. As a result, the irradiation damage of the W60-M40 alloy was more serious than that of the W70-M30 alloy but was less severe than that of the W80-M20 and W90-M10 alloys. This can be attributed to the combined effect of grain refinement, self-healing, and Ti-rich grain sputtering. This also indicates that a further homogenization of elements could improve the radiation resistance of the HE-W alloys.

Moreover, for the four HE-W alloys, some grains with less wavy structures, marked with white arrows, were flatter than the surrounding areas as shown in Fig. 4c-j. The EDS results shown in Table 6 indicate that these flatter grains are W-based grains. The generation of these special flatter W-based grains can be attributed to the effect of crystallographic orientation on the He⁺ irradiation-induced surface morphology changes [45]. During irradiation, the irradiated particles, such as H⁺ or D⁺, can be left in the material. The inventory of these

irradiated particles forms bubbles at some nucleation positions, such as voids, lattice vacancies, He clusters, and dislocations [40]. As the bubbles grow, the material surrounding the bubbles is pushed out of the surface, and then a wavy structure is formed. As the angle between the slip face and the face of the crystal grains becomes smaller, a wider, but less wavy structure is formed [46]. For W materials, the wavy structure can be easily activated along the gliding planes in a low-index slip system, such as {110} <111> system [45]. As W materials mainly slip along the {110} faces, the grains with high-index faces, that is, {103}, {407}, etc., have less wavy structures on the surface [46]. It can be concluded that flatter W-based grains have a specific crystallographic orientation.

During the irradiation test, the samples were heated by the plasma column. The temperatures of the different materials used in this work were different, as shown in Table 7. With the addition of Ta, V, Cr and Ti, the temperature of the irradiated sample increased. The thermal diffusivities of the five materials at different temperatures are shown in Fig. 5. It can be seen that at all temperatures, the thermal diffusivity decreased with an increase in the Ta, V, Cr, and Ti contents. For the HE-W alloys, the temperature of the irradiated sample correlated with the thermal diffusivity. The irradiation temperature of conventional W materials significantly affects their irradiation damage. This is because the changes in the surface morphology become more serious with an increase in temperature [8]. However, in this work, the temperature did not significantly affect the irradiation damage of the HE-W alloys. Despite its highest irradiation temperature, the irradiation damage of the W60-M40 alloy was much lower than that of W and was even slightly lower than that of the W80-M20 and W90-M10 alloys. It can be concluded that the HE-W alloys showed sufficiently high surface stability under irradiation conditions, and the effect of the irradiation temperature on the irradiation damage was not overwhelming.

Moreover, it is worth noting that previous studies on the influence of ion bombardment on the chemical stability of several distinctive W-bearing compounds, the so-called tungstates, revealed that they are rather sensitive to ion-bombardment. Such a surface ion treatment of tungstates at ion fluences comparable to those used in this study causes partial amorphization and nonstoichiometry of some elements, leading to significant changes in their binding energy values and the energy distribution of the valence electronic states. Therefore, the surfaces of the HE-W alloys were more stable than those of tungstates [47–50].

4. Conclusions

In this study, the concept of HEAs was used to develop W materials. Four HE-W alloys, W₉₀(TaVCrTi)₁₀, W₈₀(TaVCrTi)₂₀, W₇₀(TaVCrTi)₃₀, and W₆₀(TaVCrTi)₄₀, and pure W, were manufactured using mechanical alloying and SPS processes. The four HE-W alloys had the BCC structure with an ultrafine grain size. As compared to pure W, the HE-W alloys showed excellent surface stability under He⁺ irradiation, while the W₇₀(TaVCrTi)₃₀ alloy showed the best surface stability among the five materials. A 3D laser scanning confocal microscope was used to examine the surface morphology of the five materials, which was positively correlated to the damage caused by the irradiation. The higher surface stability of HE-W alloys could due to their self-healing mechanism. The ultrafine grain structure of the HE-W alloys also played an important role in improving their surface stability. The surface stability of the HE-

Table 6

EDS results of the grains marked with white arrows in Fig. 4.

Material	Figure	Composition in at.%				
		W	Ta	V	Cr	Ti
W90-M10	c	98.7	1.3	0	0	0
	d	100	0	0	0	0
W80-M20	e	85.2	3.5	3.9	5.4	1.9
	f	88.2	2.8	4	5	0
W70-M30	g	78.3	6.9	6.2	7.4	1.3
	h	80.6	7.1	4.6	6.6	1.2
W60-M40	i	65.9	12.3	9.1	10.9	1.9
	j	67.7	11.2	8.1	11	1.9

Table 7

The temperature of five materials during the irradiation test.

Material	Temperature (K)
W	~900
W90-M10	~950
W80-M20	~1010
W70-M30	~1040
W60-M40	~1100

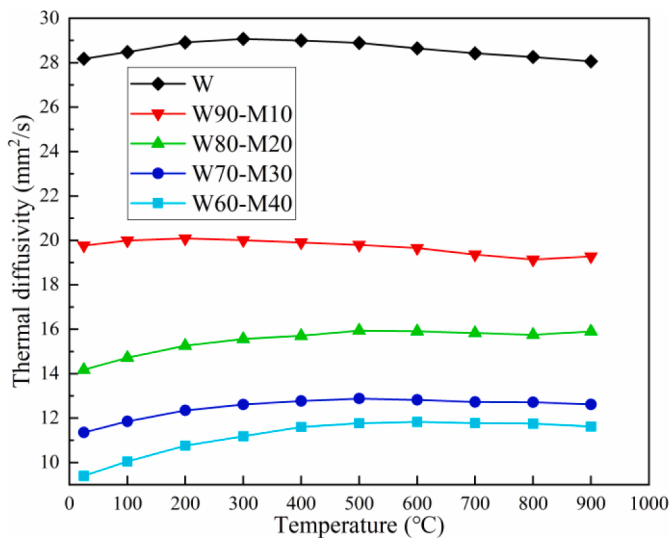


Fig. 5. Thermal diffusivity of the five materials at different temperatures.

W alloys was so strong that the effect of temperature on the irradiation damage was not significant.

CRediT authorship contribution statement

Hongjing Cui: Methodology, Investigation, Data curation, Writing – original draft. **Ning Liu:** Conceptualization, Project administration, Writing – review & editing. **Laima Luo:** Methodology. **Yue Xu:** Writing – review & editing. **Jigui Cheng:** Supervision, Writing – review & editing. **Yucheng Wu:** Resources.

Declaration of Competing Interest

The authors declare that they have no known competing financial interests or personal relationships that could have appeared to influence the work reported in this paper.

Funding sources

This work is supported by the National Natural Science Foundation of China (No. 52020105014) and Anhui International Science and Technology Cooperation Plan (No. 201904b11020034).

References

- [1] X.O. Yi, K. Arakawa, Y.F. Du, F. Ferroni, W.T. Han, P.P. Liu, F.R. Wan, High-temperature defect recovery in self-ion irradiated W-5 wt% Ta, Nucl. Mater. Energy 18 (2019) 93–98, <https://doi.org/10.1016/j.nme.2018.12.014>.
- [2] I. Smid, M. Akiba, G. Vieider, L. Plochl, Development of tungsten armor and bonding to copper for plasma-interactive components, J. Nucl. Mater. 258–263 (1998) 160–172, [https://doi.org/10.1016/s0022-3115\(98\)00358-4](https://doi.org/10.1016/s0022-3115(98)00358-4).
- [3] M. Fujitsuka, I. Mutoh, T. Tanabe, T. Shikama, High heat load test on tungsten and tungsten containing alloys, J. Nucl. Mater. 233–237A (1996) 638–644, [https://doi.org/10.1016/s0022-3115\(96\)00102-x](https://doi.org/10.1016/s0022-3115(96)00102-x).
- [4] H.D. Pacher, I. Smid, G. Federici, Y. Igithkhanov, G. Janeschitz, R. Raffray, G. Vieider, Erosion lifetime of ITER divertor plates, J. Nucl. Mater. 241–243 (1997) 255–259, [https://doi.org/10.1016/s0022-3115\(97\)80045-1](https://doi.org/10.1016/s0022-3115(97)80045-1).
- [5] G.A. Cottrell, Sigma phase formation in irradiated tungsten, tantalum and molybdenum in a fusion power plant, J. Nucl. Mater. 334 (2–3) (2004) 166–168, <https://doi.org/10.1016/j.jnucmat.2004.07.001>.
- [6] B.G. Butler, J.D. Paramore, J.P. Ligda, C. Ren, Z.Z. Fang, S.C. Middlemas, K. J. Hemker, Mechanisms of deformation and ductility in tungsten – A review, Int. J. Refract. Met. Hard Mater. 75 (2018) 248–261, <https://doi.org/10.1016/j.ijrmhm.2018.04.021>.
- [7] J.M. Steichen, Tensile properties of neutron irradiated TZM and tungsten, J. Nucl. Mater. 60 (1) (1976) 13–19, [https://doi.org/10.1016/0022-3115\(76\)90112-4](https://doi.org/10.1016/0022-3115(76)90112-4).
- [8] S. Gonderman, J.K. Tripathi, T.J. Novakowski, T. Sizyuk, A. Hassanein, The effect of low energy helium ion irradiation on tungsten-tantalum (W-Ta) alloys under fusion relevant conditions, J. Nucl. Mater. 491 (2017) 199–205, <https://doi.org/10.1016/j.jnucmat.2017.05.009>.
- [9] J. Wang, C. Li, Y. Yuan, H. Greuner, L. Cheng, G.-H. Lu, Surface modification of W-V alloy exposed to high heat flux helium neutral beams, Nucl. Fusion 58 (9) (2018), <https://doi.org/10.1088/1741-4326/aac72c>.
- [10] S. Telu, A. Patra, M. Sankaranarayana, R. Mitra, S.K. Pabi, Microstructure and cyclic oxidation behavior of W-Cr alloys prepared by sintering of mechanically alloyed nanocrystalline powders, Int. J. Refract. Met. Hard Mater. 36 (2013) 191–203, <https://doi.org/10.1016/j.ijrmhm.2012.08.015>.
- [11] F. Lukáč, M. Vilémová, B. Nevrála, J. Klecka, T. Chráška, O. Molnárová, Properties of mechanically alloyed W-Ti materials with dual phase particle dispersion, Metals 7 (1) (2016), <https://doi.org/10.3390/met7010003>.
- [12] J.W. Yeh, S.K. Chen, S.J. Lin, J.Y. Gan, T.S. Chin, T.T. Shun, C.H. Tsau, S.Y. Chang, Nanostructured high-entropy alloys with multiple principal elements: novel alloy design concepts and outcomes, Adv. Eng. Mater. 6 (5) (2004) 299–303, <https://doi.org/10.1002/adem.200300567>.
- [13] E.J. Pickering, N.G. Jones, High-entropy alloys: a critical assessment of their founding principles and future prospects, Int. Mater. Rev. 61 (3) (2016) 183–202, <https://doi.org/10.1080/09506608.2016.1180020>.
- [14] D.B. Miracle, O.N. Senkov, A critical review of high entropy alloys and related concepts, Acta Mater. 122 (2017) 448–511, <https://doi.org/10.1016/j.actamat.2016.08.081>.
- [15] Y. Zhang, Y.J. Zhou, J.P. Lin, G.L. Chen, P.K. Liaw, Solid-solution phase formation rules for multi-component alloys, Adv. Eng. Mater. 10 (6) (2008) 534–538, <https://doi.org/10.1002/adem.200700240>.
- [16] K.Y. Tsai, M.H. Tsai, J.W. Yeh, Sluggish diffusion in Co-Cr-Fe-Mn-Ni high-entropy alloys, Acta Mater. 61 (13) (2013) 4887–4897, <https://doi.org/10.1016/j.actamat.2013.04.058>.
- [17] S. Ranganathan, Alloyed pleasures: multimetalllic cocktails, Curr. Sci. 85 (10) (2003) 1404–1406.
- [18] N.A.P.K. Kumar, C. Li, K.J. Leonard, H. Bei, S.J. Zinkle, Microstructural stability and mechanical behavior of FeNiMnCr high entropy alloy under ion irradiation, Acta Mater. 113 (2016) 230–244, <https://doi.org/10.1016/j.actamat.2016.05.007>.
- [19] E.P. George, W.A. Curtin, C.C. Tasan, High entropy alloys: a focused review of mechanical properties and deformation mechanisms, Acta Mater. 188 (2020) 435–474, <https://doi.org/10.1016/j.actamat.2019.12.015>.
- [20] T. Egami, W. Guo, P.D. Rack, T. Nagase, Irradiation resistance of multicomponent alloys, Metall. Mater. Trans. A 45 (1) (2013) 180–183, <https://doi.org/10.1007/s11661-013-1994-2>.
- [21] T. Nagase, P.D. Rack, J.H. Noh, T. Egami, In-situ TEM observation of structural changes in nano-crystalline CoCrCuFeNi multicomponent high-entropy alloy (HEA) under fast electron irradiation by high voltage electron microscopy (HVEM), Intermetallics 59 (2015) 32–42, <https://doi.org/10.1016/j.intermet.2014.12.007>.
- [22] B. Savoini, J. Martínez, A. Muñoz, M.A. Monge, R. Pareja, Microstructure and temperature dependence of the microhardness of W-4V-1La2O3 and W-4Ti-1La2O3, J. Nucl. Mater. 442 (1–3) (2013) S229–S232, <https://doi.org/10.1016/j.jnucmat.2013.03.039>.
- [23] Y. Tong, D. Chen, B. Han, J. Wang, R. Feng, T. Yang, C. Zhao, Y.L. Zhao, W. Guo, Y. Shimizu, C.T. Liu, P.K. Liaw, K. Inoue, Y. Nagai, A. Hu, J.J. Kai, Outstanding tensile properties of a precipitation-strengthened FeCoNiCrTi0.2 high-entropy alloy at room and cryogenic temperatures, Acta Mater. 165 (2019) 228–240, <https://doi.org/10.1016/j.actamat.2018.11.049>.
- [24] X.-J. Yao, X.-F. Shi, Y.-P. Wang, G.-Y. Gan, B.-Y. Tang, The mechanical properties of high entropy (-like) alloy W_x(TaTiVCr)_{1-x} via first-principles calculations, Fusion Eng. Des. 137 (2018) 35–42, <https://doi.org/10.1016/j.fusengdes.2018.08.008>.
- [25] X. Yang, Y. Zhang, P.K. Liaw, Microstructure and compressive properties of NbTiVTaAlx high entropy alloys, in: Iumrs International Conference in Asia 2011 36, 2012, pp. 292–298, <https://doi.org/10.1016/j.proeng.2012.03.043>.
- [26] O.A. Waseem, J. Lee, H.M. Lee, H.J. Ryu, The effect of Ti on the sintering and mechanical properties of refractory high-entropy alloy Ti_xW_yV_zCr_w fabricated via spark plasma sintering for fusion plasma-facing materials, Mater. Chem. Phys. 210 (2018) 87–94, <https://doi.org/10.1016/j.matchemphys.2017.06.054>.
- [27] O.A. Waseem, H.J. Ryu, Powder metallurgy processing of a W_xTa_yV_zCr_w high-entropy alloy and its derivative alloys for fusion material applications, Sci. Rep. 7 (1) (2017) 1926, <https://doi.org/10.1038/s41598-017-02168-3>.
- [28] O.N. Senkov, G.B. Wilks, D.B. Miracle, C.P. Chuang, P.K. Liaw, Refractory high-entropy alloys, Intermetallics 18 (9) (2010) 1758–1765, <https://doi.org/10.1016/j.intermet.2010.05.014>.
- [29] M.S. Anzorena, A.A. Bertolo, L. Gagetti, A.J. Kreiner, H.O. Mosca, G. Bozzolo, M.F. del Grosso, Characterization and modeling of a MoTaVW_z high entropy alloy, Mater. Des. 111 (2016) 382–388, <https://doi.org/10.1016/j.matedes.2016.09.006>.
- [30] Q.Q. Wei, Q. Shen, J. Zhang, B. Chen, G.Q. Luo, L.M. Zhang, Microstructure and mechanical property of a novel ReMoTaW high-entropy alloy with high density, Int. J. Refract. Metals Hard Mater. 77 (2018) 8–11, <https://doi.org/10.1016/j.ijrmhm.2018.05.006>.
- [31] S. Das, P.S. Robi, Mechanical alloying of W-Mo-V-Cr-Ta high entropy alloys, in: International Conference on Recent Advances in Materials & Manufacturing Technologies 346, 2018, <https://doi.org/10.1088/1757-899x/346/1/012047>.
- [32] Z.D. Han, H.W. Luan, X. Liu, N. Chen, X.Y. Li, Y. Shao, K.F. Yao, Microstructures and mechanical properties of Ti NbMoTaW refractory high-entropy alloys, Mater. Sci. Eng. A 712 (2018) 380–385, <https://doi.org/10.1016/j.msea.2017.12.004>.
- [33] I. Kunce, M. Polanski, J. Bystrzycki, Microstructure and hydrogen storage properties of a TiZrNbMoV high entropy alloy synthesized using Laser Engineered Net Shaping (LENS), Int. J. Hydrog. Energy 39 (18) (2014) 9904–9910, <https://doi.org/10.1016/j.ijhydene.2014.02.067>.
- [34] B. Vishwanadh, N. Sarkar, S. Gangil, S. Singh, R. Tewari, G.K. Dey, S. Banerjee, Synthesis and microstructural characterization of a novel multicomponent

- equiatomic ZrNbAlTiV high entropy alloy, *Scr. Mater.* 124 (2016) 146–150, <https://doi.org/10.1016/j.scriptamat.2016.07.018>.
- [35] O.N. Senkov, J.M. Scott, S.V. Senkova, D.B. Miracle, C.F. Woodward, Microstructure and room temperature properties of a high-entropy TaNbHfZrTi alloy, *J. Alloys Compd.* 509 (20) (2011) 6043–6048, <https://doi.org/10.1016/j.jallcom.2011.02.171>.
- [36] O.N. Senkov, G.B. Wilks, J.M. Scott, D.B. Miracle, Mechanical properties of Nb25Mo25Ta25W25 and V20Nb20Mo20Ta20W20 refractory high entropy alloys, *Intermetallics* 19 (5) (2011) 698–706, <https://doi.org/10.1016/j.intermet.2011.01.004>.
- [37] Y. Xu, Y. Xu, Z. Wu, L. Luo, X. Zan, G. Yao, Y. Xi, Y. Wang, X. Ding, H. Bi, X. Zhu, Q. Xu, J. Wu, Y. Wu, Plasma-surface interaction experimental device: PSIEC and its first plasma exposure experiments on bulk tungsten and coatings, *Fusion Eng. Des.* 164 (2021), <https://doi.org/10.1016/j.fusengdes.2020.112198>.
- [38] O. El-Atwani, S. Gonderman, M. Efe, G. De Temmerman, T. Morgan, K. Bystrøv, D. Klenosky, T. Qiu, J.P. Allain, Ultrafine tungsten as a plasma-facing component in fusion devices: effect of high flux, high fluence low energy helium irradiation, *Nucl. Fusion* 54 (8) (2014), <https://doi.org/10.1088/0029-5515/54/8/083013>.
- [39] O. El-Atwani, J.A. Hinks, G. Greaves, J.P. Allain, S.A. Maloy, Grain size threshold for enhanced irradiation resistance in nanocrystalline and ultrafine tungsten, *Mater. Res. Lett.* 5 (5) (2017) 343–349, <https://doi.org/10.1080/21663831.2017.1292326>.
- [40] O. El-Atwani, K. Hattar, J.A. Hinks, G. Greaves, S.S. Harilal, A. Hassanein, Helium bubble formation in ultrafine and nanocrystalline tungsten under different extreme conditions, *J. Nucl. Mater.* 458 (2015) 216–223, <https://doi.org/10.1016/j.jnucmat.2014.12.095>.
- [41] T. Nagase, A. Nino, T. Hosokawa, Y. Umakoshi, Electron irradiation induced crystal-to-amorphous-to-crystal transition in some metallic glasses, *Mater. Trans.* 48 (7) (2007) 1651–1658, <https://doi.org/10.2320/matertrans.MJ200701>.
- [42] T. Nagase, Y. Umakoshi, Phase stability of amorphous and crystalline phases in melt-spun Zr66.7Cu33.3 alloy under electron irradiation, *Scr. Mater.* 48 (9) (2003) 1237–1242, [https://doi.org/10.1016/s1359-6462\(03\)00056-3](https://doi.org/10.1016/s1359-6462(03)00056-3).
- [43] S. Anada, T. Nagase, H. Yasuda, H. Mori, Electron-irradiation-induced phase transition in Cr2M (M = Ti and Al) intermetallic compounds, *J. Alloys Compd.* 579 (2013) 646–653, <https://doi.org/10.1016/j.jallcom.2013.06.122>.
- [44] W. Sinkler, D.E. Luzzi, C.W. Allen, Electron irradiation of TiM2 Laves compounds: the influence of beta phase stability on amorphization, *Scr. Metall. Mater.* 28 (7) (1993) 863–868, [https://doi.org/10.1016/0956-716x\(93\)90367-2](https://doi.org/10.1016/0956-716x(93)90367-2).
- [45] S. Lindig, M. Balden, V.K. Alimov, T. Yamanishi, W.M. Shu, J. Roth, Subsurface morphology changes due to deuterium bombardment of tungsten, *Phys. Scr. T138* (2009), <https://doi.org/10.1088/0031-8949/2009/138/014040>.
- [46] N. Ohno, Y. Hirahata, M. Yamagawa, S. Kajita, M. Takagi, N. Yoshida, R. Yoshihara, T. Tokunaga, M. Tokitani, Influence of crystal orientation on damages of tungsten exposed to helium plasma, *J. Nucl. Mater.* 438 (2013) S879–S882, <https://doi.org/10.1016/j.jnucmat.2013.01.190>.
- [47] V.V. Atuchin, L.D. Pokrovsky, O.Y. Khyzhun, A.K. Sinelnichenko, C.V. Ramana, Surface crystallography and electronic structure of potassium yttrium tungstate, *J. Appl. Phys.* 104 (3) (2008), <https://doi.org/10.1063/1.2963957>.
- [48] V.L. Bekenev, O.Y. Khyzhun, V.V. Atuchin, Electronic structure of monoclinic α -KY (WO_4)₂ tungstate as determined from first-principles FP-LAPW calculations and X-ray spectroscopy studies, *J. Alloys Compd.* 485 (1–2) (2009) 51–58, <https://doi.org/10.1016/j.jallcom.2009.06.112>.
- [49] V.V. Atuchin, E.N. Galashov, O.Y. Khyzhun, A.S. Kozhukhov, L.D. Pokrovsky, V. N. Shlegel, Structural and electronic properties of $ZnWO_4$ (010) cleaved surface, *Cryst. Growth Des.* 11 (6) (2011) 2479–2484, <https://doi.org/10.1021/cg200265p>.
- [50] V.V. Atuchin, E.N. Galashov, O.Y. Khyzhun, V.L. Bekenev, L.D. Pokrovsky, Y. A. Borovlev, V.N. Zhdankov, Low thermal gradient Czochralski growth of large $CdWO_4$ crystals and electronic properties of (010) cleaved surface, *J. Solid State Chem.* 236 (2016) 24–31, <https://doi.org/10.1016/j.jssc.2015.05.017>.